High-throughput magnetic co-doping and design of exchange interactions in topological insulators

Rubel Mozumder [1], Johannes Wasmer [1,2] David Antognini Silva [1,2] Stefan Blügel [1] and Philipp Rüßmann [1,3,*]
[1] Peter Grünberg Institut (PGI-1), Forschungszentrum Jülich and JARA, 52425 Jülich, Germany
[2] Institute for Theoretical Physics, RWTH Aachen University, 52074 Aachen, Germany
[3] Institute of Theoretical Physics and Astrophysics, University of Würzburg, 97074 Würzburg, Germany

(Received 5 July 2024; accepted 19 September 2024; published 17 October 2024)

Using high-throughput automation of *ab initio* impurity embedding simulations, we create a database of 3*d* and 4*d* transition metal defects embedded into the prototypical topological insulators (TIs) Bi_2Te_3 and Bi_2Se_3. We simulate both single impurities as well as impurity dimers at different impurity-impurity distances inside the topological insulator matrix. We extract changes to magnetic moments, analyze the polarizability of nonmagnetic impurity atoms via nearby magnetic impurity atoms and calculate the exchange coupling constants for a Heisenberg Hamiltonian. We uncover chemical trends in the exchange coupling constants and discuss the impurities' abilities with respect to magnetic order in the fields of quantum anomalous Hall insulators and topological quantum computing. In particular, we confirm that co-doping of different magnetic dopants is a viable strategy to engineer the magnetic ground state in magnetic TIs.

DOI: 10.1103/PhysRevMaterials.8.104201

I. INTRODUCTION

In recent years, Topological insulators (TIs) have emerged as a revolutionary class of materials, characterized by an insulating bulk and conducting surface states protected by time-reversal symmetry [1]. Breaking time-reversal symmetry in TI materials by magnetic doping turns them into so-called magnetic TIs (MTIs) [2,3], where exotic quantum phenomena such as the quantum anomalous Hall (QAH) effect are found [4–8], leading to the possibility of dissipationless transport by the edge states in the absence of a magnetic field [9]. Pioneering experimental realization of the QAH effect in MTI was achieved by Cr-doped [4] and V-doped [5] $(Bi, Sb)_2Te_3$, where quantized transport was seen at temperatures ($T < 100\,\mathrm{mK}$). The low critical temperature for the QAH effect remains an open challenge that is attacked by different strategies. On the one hand, new stoichiometric materials like $MnBi_2Te_4$ [10], or transition metal dichalcogenide van der Waals heterostructures are explored [11]. On the other hand, in MTIs, modulation doping [12] or co-doping strategies [13] are viable options to raise the critical temperature of QAH materials.

Aside from the QAH phase, MTIs have great potential for spintronics [14], and offer the possibility of realizing the axion insulator state that, in contrast to the QAH phase, relies on antiferromagnetic order [9,15,16]. Furthermore, in the emerging field of topological superconductivity, combining topological electronic structures with magnetic doping and superconductivity is a pathway toward topological superconducting materials with possibilities for fault-tolerant quantum computing architectures [2].

Thus, controlling the magnetic properties of MTIs, e.g., the size of the exchange splitting or the long-range magnetic ordering of the magnetic atoms, poses a materials optimization challenge that is addressed in this paper. Based on high-throughput *ab initio* impurity embedding calculations [17], we simulate transition metal defects and dimers of impurities embedded into the prototypical TIs Bi_2Te_3 and Bi_2Se_3, thus extending the JuDiT database [18] of calculated impurity properties embedded into topological insulators [17] with co-doping of impurity dimers. Using density functional theory (DFT) simulations, we calculate their magnetic properties, the exchange coupling constant at different impurity distances that map the magnetic interactions onto a classical Heisenberg Hamiltonian, and discuss the influence of co-doping on the magnetic order. Overall, our database includes several thousand impurity dimer calculations.

The paper is organized as follows. In Sec. II the computational methodology is introduced. Then, in Sec. III, the results of the impurity database of this work is presented and discussed. Finally, Sec. IV concludes the paper with a summary and an outlook.

II. METHODS

A. *Ab initio* impurity embedding

The DFT results of this work are produced within the local density approximation (LDA) [19] using the full-potential relativistic Korringa-Kohn-Rostoker Green's function method (KKR) [20] as implemented in the `JuKKR` code package [21]. This approach has previously shown its good agreement with

*Contact author: p.ruessmann@fz-juelich.de

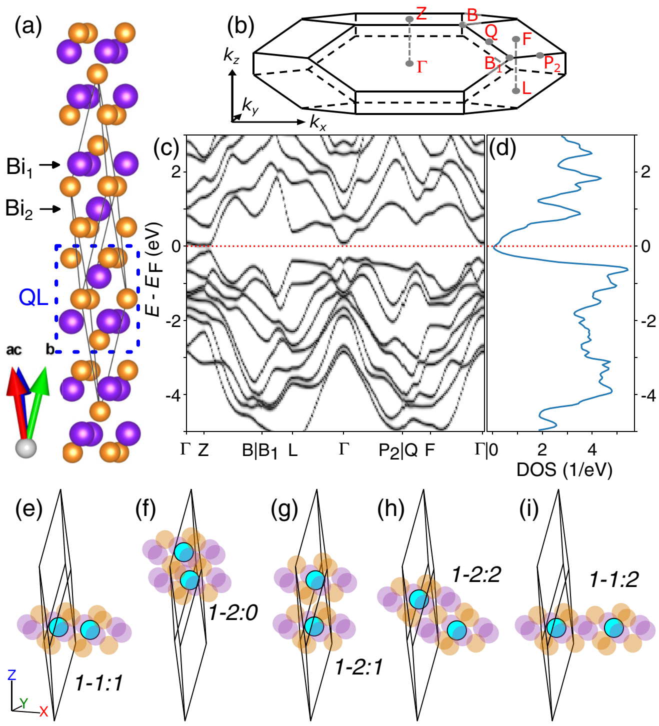

FIG. 1. Calculation setup. (a) Crystal structure of the Bi_2Te_3 host crystal, where the quintuple layer (QL) structure with the two equivalent Bi sites Bi_1, Bi_2 is highlighted. (c) Electronic band structure along paths connecting the high-symmetry points indicated in the Brillouin zone in (b) and (d) corresponding density of states. (e)–(i) Double-impurity clusters for increasing distances between the impurities ($R = 4.38$ Å, 4.79 Å, 6.10 Å, 6.49 Å, 7.59 Å). The impurity atoms (blue) are substituting $Bi_{1/2}$ as indicated by the labels of the form "$\mu - \nu : o$" where μ, ν indicate the Bi layer and o indexes the shell of nearest-neighbor distance.

various experimental observables in the past, e.g., scattering properties measured by scanning tunneling microscopy (STM) [22], impurity properties measured with resonant photoemission spectroscopy ((resPES) [23], or x-ray magnetic circular dichroism (XMCD) [24]. We use the experimental crystal structure of bulk Bi_2Te_3 [25] and Bi_2Se_3 [26] shown in Fig. 1(a). Throughout this work, we use an $\ell_{max} = 3$ cutoff in the angular momentum expansion with an exact description of the atomic cells [27,28], and we use an energy contour in the integration of the charge density with 63 complex-valued energy points and a 40^3 k-points in the Brillouin zone integration of the self-consistent calculations. The error in the charge density integration arising from the finite ℓ_{max} cutoff is corrected using Lloyd's formula [29]. This leads to a bulk insulating Bi_2Te_3 host crystal as shown in the electronic band structure and corresponding DOS in Figs. 1(b)–1(d). All our calculations include the effect of spin-orbit coupling (SOC) self-consistently, which is essential to reproducing the inverted (i.e., topological) band structure of Bi_2Te_3 around the Γ point. The corresponding electronic structure of the Bi_2Se_3 crystal is shown in the Supplemental Material [30].

The Green function formulation of the KKR method allows including the impurities efficiently into crystalline solids [20,31] which, in this work, is done for $3d$ and $4d$ transition metal impurities substituting Bi sites that occupy equivalent Wyckoff sites in the pristine crystal structure of Bi_2Te_3 and Bi_2Se_3, as shown in Fig. 1. Here, we make use of the Dyson equation

$$G^{\text{imp}} = G^{\text{host}} + G^{\text{host}} \Delta V G^{\text{imp}}, \tag{1}$$

where G^{host} is the Green function of the crystalline host system, $\Delta V = V^{\text{imp}} - V^{\text{host}}$ is the difference in the potential introduced due to the presence of the impurity, and G^{imp} is the Green function that describes the impurity embedded into the periodic host crystal. Importantly, the change in the potential, ΔV, occurs only in a small region around the impurity. Thus, the Dyson equation can be solved in a small real-space area around the impurity site called the impurity cluster. Having neighboring host atoms included in the impurity cluster is, however, required for a proper charge screening of the embedded impurity. In our work, the impurity cluster contains all atoms within a cutoff radius of 4.5 Å, i.e., including the first three neighboring shells of host atoms. For the impurity embedding step and the subsequent calculation of the J_{ij} parameters (cf. Eq. (2)), we increase the k-point integration grid in the calculation of G^{host} for Eq. (1) to 100^3 k points. As shown in the Supplemental Material [30], this results in a mean absolute error of the J_{ij} values of only 2 μeV.

B. Extended Heisenberg Hamiltonian

The focus of this work is the evaluation of the magnetic properties of $3d$ and $4d$ transition metal impurities in Bi_2Te_3 in the limit of low impurity concentrations, the relevant regime for turning TIs into Chern insulators. In this regime, we can exclude any change of the structural symmetry of the TI host crystal. Therefore, our impurity embedding focuses on dimers of impurity atoms at different distances, illustrated in Figs. 1(e)–1(f). These DFT calculations for impurity dimers are then mapped onto the Heisenberg Hamiltonian to describe the magnetic interactions among impurities in the form

$$H = -\frac{1}{2} \sum_{i,j} J_{ij} \mathbf{S}_i \cdot \mathbf{S}_j. \tag{2}$$

Here, i, j label the magnetic atoms at different distances corresponding to the connecting vectors $\mathbf{R}_{ij} = \mathbf{R}_j - \mathbf{R}_i$, $\mathbf{S}_i = \mathbf{m}_i/|\mathbf{m}_i|$ denotes the unit vector indicating the direction of the magnetic moment $\mathbf{m}_i$ at site i, and J_{ij} is the isotropic exchange interaction that is responsible for the long-range magnetic ordering discussed in Sec. III D. The Green function formulation of KKR allows the calculation of the exchange parameters directly from the DFT electronic structure of impurity dimers using the method of infinitesimal rotations [32]. In this work, we are modeling random distributions of impurity atoms within the TI host crystal at low impurity concentrations that neglect structural changes to the host crystal. This random orientation will lead to an averaging out of directional Dzyaloshinskii-Moriya interaction (DMI) that would otherwise require including additional terms of the form $\mathbf{D}_{ij} \cdot (\mathbf{S}_i \times \mathbf{S}_j)$ in the Heisenberg Hamiltonian and which favor a canting of spins and noncollinear spin textures. Since we assume that the DMI will average out over the random impurity configurations, we focus our analysis on changes of the impurities' magnetic moments and on their J_{ij} parameters.

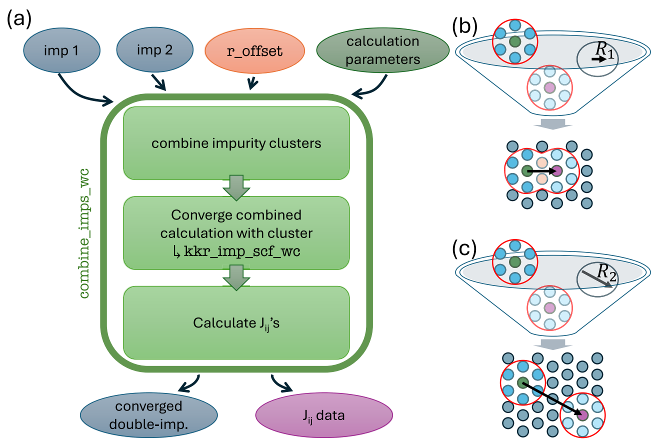

FIG. 2. AiiDA workflow to combine impurity calculations to larger clusters. (a) Outline of the `combine_imps_wc` workchain of the AiiDA-KKR plugin. Based on two impurities as input together with a definition of the offset vector between the impurities (`r_offset`), the workflow first combines the impurity clusters into one larger impurity cluster that is embedded into the host crystal in a self-consistent calculation, making use of the `kkr_imp_scf_wc` workchain, before finally the J_{ij} parameters are extracted in a post-processing step. (b), (c) Illustration of two inputs to the `combine_imps_wc` workchain for different offset vectors $\boldsymbol{R}$. For small $\boldsymbol{R}$, the single-impurity embedding clusters might overlap where duplicate positions [orange sites in (b)] are removed before the self-consistent DFT calculation for the dimer is pursued.

C. High-throughput workflow

We consider all 20 impurity dimers of $3d$ and $4d$ impurities up to a distance of 12.5 Å between the two impurities. Figures 1(e)–1(i) and Fig. A1 in the Supplemental Material [30] illustrate the geometry of the impurity dimers we include in this study. For each impurity dimer at a given distance, $20 \times 21/2 = 210$ unique impurity dimers need to be calculated self-consistently to take into account possible charge transfer between the impurities that can influence the impurities' magnetic properties. This results in a large number of self-consistent DFT calculations for dimers at different distances and the subsequent extraction of J_{ij} parameters. At larger distances, we restrict our calculations to pairs of impurities that are magnetic in the single impurity limit, where $|m| > 10^{-3}\mu_B$. Overall, we calculate more than 2600 unique impurity dimers and extract their exchange coupling parameters.

The large number of DFT calculations in this study are therefore conveniently orchestrated using the AiiDA-KKR [17,33] plugin to the AiiDA high-throughput infrastructure [34], where we used the `submission_controller` of AiiDA-JuTools in the workload management [35]. For this purpose, we have extended the capabilities of AiiDA-KKR with a new workflow called `combine_imps_wc`, which is sketched in Fig. 2. This workflow is capable of starting from two impurity calculations. It combines them into a larger impurity cluster, converges the DFT calculation for this combined cluster, and, finally, extracts the J_{ij} parameters. The `combine_imps_wc` workflow is also capable of extending an impurity cluster consisting of a dimer or more impurity atoms, by adding another impurity cluster. In this way, small nanostructures of impurities can be constructed and embedded self-consistently into the host crystal.

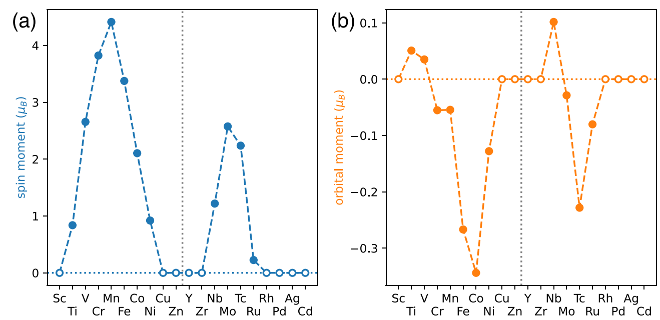

FIG. 3. Single impurity magnetic (a) spin- and (b) orbital moments for $3d$- and $4d$-impurities embedded as substitutional defects on Bi sites in Bi_2Te_3.

III. RESULTS AND DISCUSSION

We focus the following detailed analysis on the results of impurities in Bi_2Te_3. We believe that our conclusions can be transferred to other TIs of the same family, e.g., Bi_2Se_3 or Sb_2Te_3, which is discussed in the subsection III E.

A. Single-impurity properties

Figure 3 summarizes the magnetic moments of single impurities embedded as substitutional defects on Bi sites within bulk Bi_2Te_3. Going through the $3d$ and $4d$ series of transition metal impurities, we find that the $3d$ impurities from V to Co and the $4d$ impurities from Nb to Ru have a magnetic ground state where the magnetic moments reach a maximum following the well-known trends with the increasing occupation of the d shell of the impurities. The orbital moment generally follows Hund's rules with a sign change from positive to negative orbital moment for increasing d-shell filling.

Figure 4 summarizes the single impurity density of states for all 20 $3d$ and $4d$ defects in Bi_2Te_3. Some impurities show resonances of the d states around the Fermi energy like V, Cr, Fe, and Co from the $3d$ series and Nb, Tc, or Pd from the $4d$ series. This is in line with earlier calculations for impurities in Sb_2Te_3 and it can be important in the materials optimization procedure when designer properties (such as a low DOS at the Fermi energy) are desirable [17]. From the difference in the position of the dominant peak in the minority and majority spin channels of the DOS, we estimate the size of the exchange splitting Δ_{xc} of the different impurities. This is summarized in Fig. 4(c) where we recover the same trend of Δ_{xc} with the d shell as in the size of the spin moments (cf. Fig. 5). The largest Δ_{xc} is found for Mn where the spin moment is also maximal. Within the series of $4d$ impurity elements the magnitude of the exchange splitting is smaller. Thus, using $4d$ dopants such as Mo can combine a low DOS at the Fermi level with a sizable spin moment and moderate exchange splitting. This can be beneficial in the materials optimization challenge around magnetic TIs proximitized by a superconductor in the field of topological quantum computing [36,37].

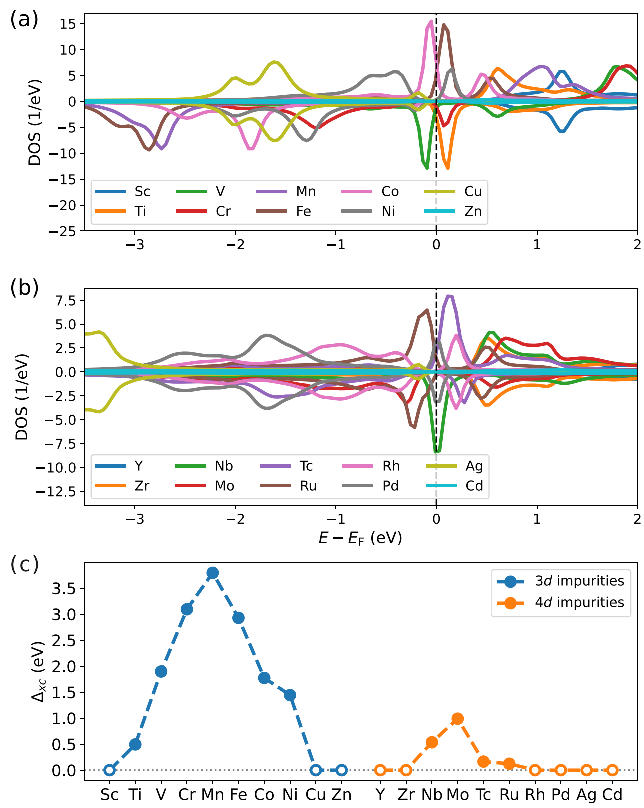

FIG. 4. Density of states of single substitutional M_{Bi} defects in Bi_2Te_3 for (a) $M = 3d$ and (b) $M = 4d$ impurities. The minority (majority) spin channel is shown with a positive (negative) sign of the DOS. (c) Size of the exchange splitting Δ_{xc} extracted from the energy difference between the maxima of minority and majority spin channels.

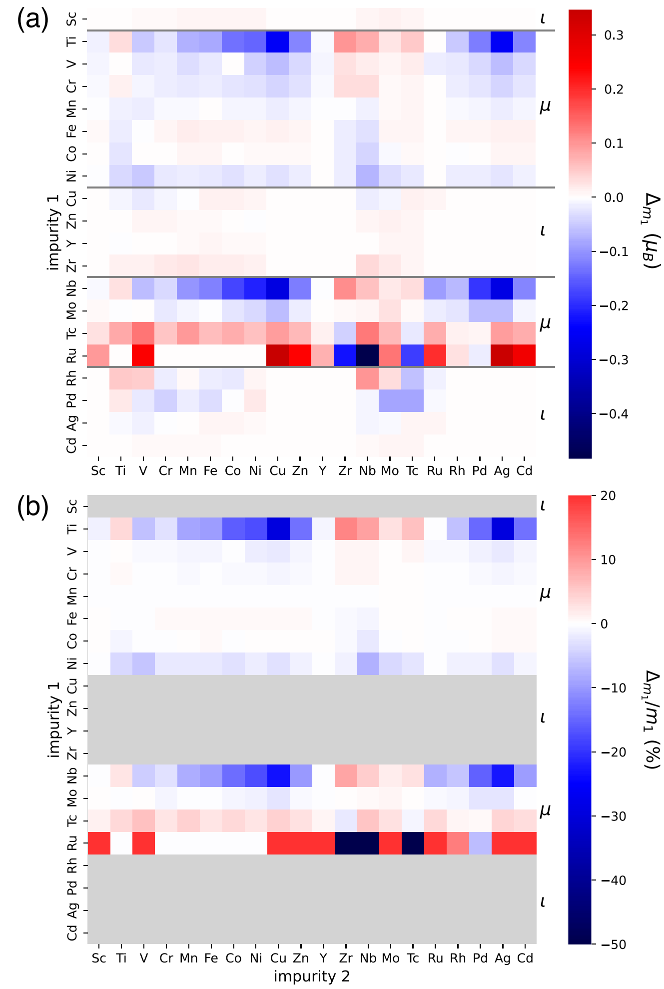

FIG. 5. Changes in the magnetic moments for nearest-neighbor impurities ($R = 4.38$Å) in Bi_2Te_3. (a) Absolute change Δ_{m_1} in μ_B of the spin moment of impurity 1 upon adding impurity 2 and (b) corresponding relative change in %. The gray horizontal lines and the symbols ι (μ) label nonmagnetic (magnetic) impurities in the isolated single impurity case meaning that the magnetic moment change given for ι impurities denote induced moments due to nearest-neighbor magnetic atoms.

B. Co-doping-induced changes of the magnetic moments and polarizability

The effect of co-doping on the magnetic moments of impurities is shown in Fig. 5 where the absolute and relative change in the spin magnetic moment for nearest neighbor impurities is shown in panels (a), (b), respectively. We find changes to the magnetic moments of impurity 1 Δm_1 due to the presence of impurity 2 that reach $0.5\mu_B$ in magnitude. Magnetic impurities (marked by the symbol μ in Fig. 5) show larger changes to their magnetic moments where the largest changes are seen for impurities with weak magnetic moments of isolated single impurities like Ti ($m = 0.84\mu_B$, max $|\Delta m_1| = 0.25\mu_B$), Nb ($1.22\mu_B$, $0.28\mu_B$), or Ru ($0.23\mu_B$, $0.48\mu_B$) [38]. Magnetic impurities from the middle of the $3d$ series that show large magnetic moments (V to Co) are only weakly affected as seen from the small relative change of $\leqslant 2\%$ in the magnetic moments shown in Fig. 5(b). Furthermore, similarities between the Ti and Nb suggest that a similar filling of the valence d shell can explain the chemical trends that we observe.

Initially, nonmagnetic impurities (marked by the symbol ι in Fig. 5) can be polarized by the presence of nearby magnetic defects, which is particularly pronounced for Rh and Pd with induced moments reaching magnitudes of $0.1\mu_B$ for nearby Nb, Mo, or Tc atoms. A positive (negative) sign of the induced moment then indicates parallel (antiparallel) alignment of the spins in the two impurity atoms. The high polarizability correlates with a peak in the DOS close to the Fermi energy as shown by the pink (gray) curves in Fig. 4(b) for Rh (Pd).

C. Distance-dependent exchange coupling constants

Figure 6 shows maps of the J_{ij} couplings for all impurity dimers of $3d$ and $4d$ dopants at the first five distances between 4.4 Å and 7.5 Å (cf. Supplemental Material Fig. A2 for larger distances [30]). As expected, dimers with nonmagnetic impurities (e.g., Sc, Cu, Zn, Y, Zr, Rh, Pd, Ag, and Cd) lead to vanishing exchange couplings which serve as a consistency check for our method. Overall, we find clear chemical trends following the d-orbital filling of the magnetic dopants. This can be seen, for instance, in the red-to-blue color change that

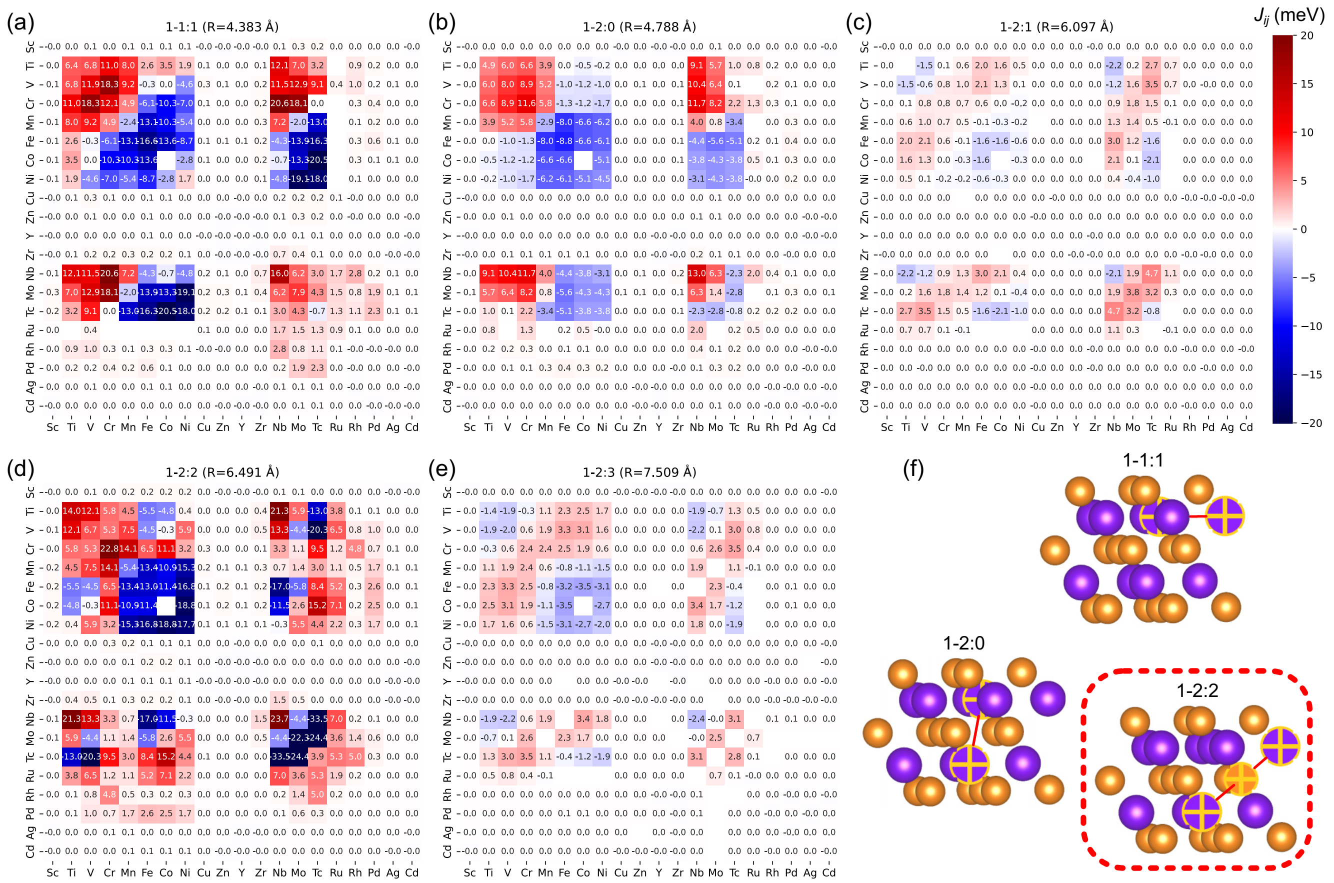

FIG. 6. Pairwise Heisenberg exchange coupling parameters J_{ij} for (a)–(e) the first five impurity-impurity distances in Bi_2Te_3 where the impurities are from the 3d ($Z_{imp} = 21 - 30$, i.e., Sc to Zn) and 4d ($Z_{imp} = 39 - 48$, i.e., Y to Cd) series. (f) Visualization of the three impurity dimer configurations that lead to the largest exchange coupling constants (shown in a,b,d), which are among substitutional Bi sites (labeled Bi_1 and Bi_2, cf. Fig. 1) within the same Bi_2Te_3 quintuple layer. The highlighted configuration (1–2:2) shows the largest magnitude of the J_{ij} values due to the linear Bi_1–Te–Bi_2 geometry maximizing the electronic interactions between impurities at these sites.

indicates a sign change when following the diagonal within the block of magnetic 3d impurities (i.e., from Ti to Ni) in panels (a), (b). However, at larger distances, we find two sign changes from $J_{ij} < 0$ to $J_{ij} > 0$ and back to $J_{ij} < 0$ as seen in panels (c), (e). Similar trends are visible for dimers within the 4d block of dopants, where, however, fewer impurities are magnetic to begin with. Also, the co-doping of 3d with 4d impurities follows this trend.

With increasing distances, the magnitude of the J_{ij}'s generally decay but then suddenly recover to large values of $|J_{ij}| \geqslant 20$ meV again at a distance of 6.5 Å shown in Fig. 6(d). A close inspection of the impurity dimer in real space for the fourth neighbor reveals its special character. As illustrated in Fig. 6(f), the substitutional Bi sites of this dimer lie on a straight line with an additional Te atom in between. This special geometry can lead to the Kramers-Anderson superexchange mechanism where the exchange interaction is mediated by virtual electron hoppings from the first impurity to the nonmagnetic Te site and then onward to the second impurity [39]. Following the Goodenough-Kanamori rule, this superexchange mechanism is maximal for 180° orientations between the substitutional impurities on Bi sites in the Bi_1-Te-Bi_2 configuration.

A closer analysis reveals an oscillating sign of the exchange interactions as seen, for instance, for Ti–Ti dimers with two sign changes from positive to negative (and vice versa) within the first five neighbors. This can be attributed to a competition of different exchange mechanisms including direct exchange of overlapping impurity states at short distances, superexchange for the 4th neighbor, and RKKY-like oscillatory behavior for larger distances [23].

Figure 7 shows the distance dependence of the J_{ij}'s for all combinations of magnetic impurities included in our study. We find both positive and negative values for the exchange coupling depending on the type and the distance between impurities in the dimers. Generally, there is an overall decay of the magnitude of J_{ij} with distance as shown in the inset of Fig. 7 where the maximal absolute value of the J_{ij} at a given distance between the impurities is shown. We find a striking outlier to this general trend for the fourth neighbor ($R_{ij} = 6.5$ Å) where the largest overall values are found despite the large distance between the impurities due to the 180° alignment discussed above. Neglecting the outlier of the fourth neighbor, we can characterize the decay of the magnitude of the J_{ij}'s well with an exponential function of the form $J(R) = J_0 \cdot e^{-R/\lambda}$ with $J_0 = 215.2$ meV and $\lambda = 1.79$ Å.

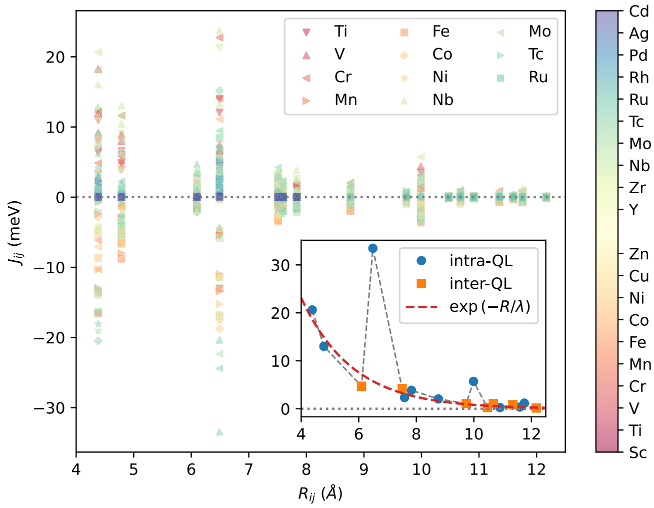

FIG. 7. Decay of the Heisenberg exchange coupling constants among impurities in Bi_2Te_3 with distance. The symbols indicate the type of atom i and the colors the type of atom j of the respective J_{ij} pairs. The inset shows the maximal absolute value for each shell where the color of the symbol indicates couplings within the same quintuple layer (intra-QL, circles) or from one to the next (inter-QL, squares) quintuple layer above or below. The red dashed line in the inset shows a fit for an exponential decay (neglecting the outlier at the maximal value at $R_{ij} = 6.49$ Å) giving a decay constant of $\lambda = 1.79$ Å.

D. Long-range magnetic ordering

Finally, as a way to estimate the collective magnetic ordering for a given impurity configuration, we compute the critical temperature in mean-field approximation [40]

$$T_c = \frac{1}{3} k_B \sum_{j>0} c_j J_{0,j}, \tag{3}$$

where the sum over the pairs j counts all equivalent pairs within shells at constant R_{ij} and c_j are the concentrations of magnetic impurities at site j (i.e., with magnetic moments $m_{i,j} \geqslant 10^{-3}\mu_B$) which considered distances of $R_{ij} \leqslant 12.5$ Å [41]. Figure 8 shows the convergence of the T_c together with the contributions of the J_{ij}'s arising from the different shells for V–Cr co-doping in Bi_2Te_3. The overall exponential decay of the J_{ij}'s counteracts the increasing number of neighbors in the shells at greater distances, which leads to a slow convergence of the critical temperature with distance between impurities. It is therefore essential to include large distances of $R_{ij} \geqslant 10$ Å in this analysis. The convergence of the T_c and the exponential decay of the decaying envelope of the J'_{ij}s with distance result in an estimated error of the computed T_c in the order of $J(R_{ij} = 12.5\,\text{Å}/J(R_{ij} = 0) = e^{-12.5\text{Å}/\lambda} < 10^{-3}$ (with $\lambda = 1.79$ Å, cf. Fig. 7). This gives us *a posteriori* justification for this chosen cutoff in our computational setup.

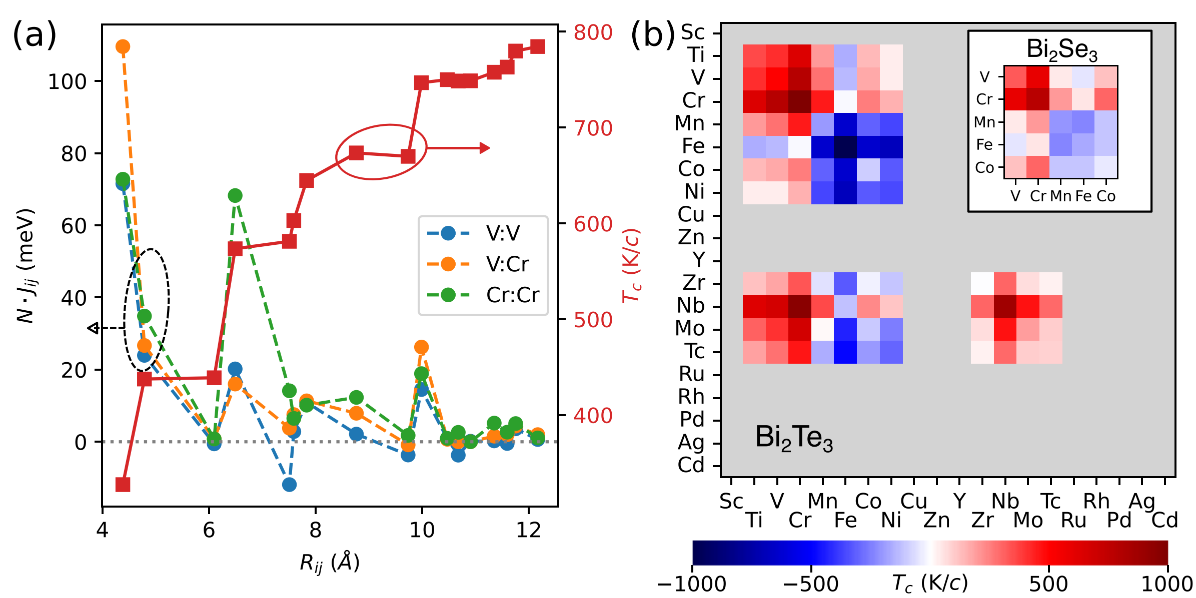

FIG. 8. Tendency for long-range magnetic order estimated by the mean-field ordering temperature in magnetically doped Bi_2Te_3. (a) Convergence of the mean-field critical temperature [Eq. (3)] as function of the distance between two V and/or Cr impurities leading to $T_c = 784.5$ K/c (assuming equal impurity concentrations $c = c_i = c_j$ for V and Cr). Broken lines report the pairwise J_{ij}'s multiplied by the number of atoms per shell and full lines indicate the T_c as function of the distance between the impurity atoms. (b) Map of the resulting estimate for the mean-field T_c for all impurity combinations assuming equal concentration of both impurity types ($c = c_i = c_j$) as described in the main text. Note that a positive (negative) T_c indicates the tendency for ferromagnetic (antiferromagnetic) long-range ordering. Gray areas indicate non magnetic impurities at site i and/or j leading to a vanishing set of J_{ij}'s. The inset in (b) shows the mean-field T_c for $3d$ dopants in Bi_2Se_3.

For simplicity, we assume equal concentration of the two impurity kinds at sites i and j in the calculation of the T_c. Therefore, we simply average the T_c arising from the different impurity-impurity configurations in the case of co-doping of two kinds of impurities. For instance, to describe V–Cr alloys, we calculate $T_c = (T_c[\mathrm{V}-\mathrm{V}] + T_c[\mathrm{Cr}-\mathrm{Cr}] + T_c[\mathrm{V}-\mathrm{Cr}])/3$. Figure 8(b) shows the resulting map of the T_c's where the blue color indicates negative T_c (antiferromagnetic ordering) while red colors indicate positive T_c (ferromagnetic).

Co-doping can be a viable strategy to increase the stability of a desired magnetic order as demonstrated by the Cr–V co-doped configuration. This is evident from the contributions to the converged T_c for V–Cr pairs that show larger couplings for nearest neighbors as well as for the 10th neighbor that would be important at large (small) impurity concentrations when nearest (far away) neighbors contribute more to the magnetic ordering due to the difference in the average impurity distance with concentration.

Overall, we find the largest positive T_c values for Cr impurities which is also a well-known QAH material [4,9]. Typical V- and Cr-doped TIs show magnetic ordering temperatures between 10 and 40 K, depending on the concentration of magnetic atoms (M) which typically lies in the range of $c = 10 - 20\%$ for $(M_c\mathrm{Bi}_{1-c})_2\mathrm{Te}_3$ [9,42,43]. Using these concentrations we arrive at an estimated mean-field ordering temperature of $T_c = 50 - 200\,\mathrm{K}$. The overestimation of the T_c compared to experimental observations is a known deficiency of the mean-field approximation which, especially in the limit of dilute magnetic dopants, exaggerates the contribution of nearest neighbor impurity dimers that only occur seldom at low concentrations. In contrast, larger distances between impurities become more important where the pronounced local maxima at the fourth and 10th neighbors would stabilize more long-range magnetic order and lead to lower percolation thresholds and a more stable long-range magnetic order. All these effects are not included in the crude mean-field approximation we apply here, which only serves as a rough estimate allowing us to judge the general tendency for magnetic ordering in these materials.

The tendency to overestimate the influence of short impurity distances is seen in a quantitative comparison of the mean-field estimate for the T_c when the nearest neighbor contributions are neglected [44]

$$T_c' = \frac{1}{3} k_B \sum_{j>1} c J_{0,j}. \tag{4}$$

For Cr, this leads to a moderate improvement in the estimated ordering temperature from $T_c/T_c^{\mathrm{exp}} = 5.5$ to $T_c'/T_c^{\mathrm{exp}} = 4$ with $T_c^{\mathrm{exp}} = 40\,\mathrm{K}$ for an impurity concentration of $c = 22\%$ [43]. For Mn impurities, our estimation from the mean-field approach even predicts antiferromagnetic ordering which disagrees with the small ferromagnetic ordering temperature of 10 K at $c = 9\%$ found in experiments [45]. We speculate that this discrepancy could be related to different trends in the inter-QL vs. intra-QL exchange parameters (cf. Supplemental Material Fig. A3 [30]) where we find a sign change for Mn. As shown in the Supplemental Material in Fig. A4 [30], the summation of the inter-QL J_{ij}'s results in a ferromagnetic ordering of the Mn atoms from different QLs, while the intra-QL ordering favors antiferromagnetic alignment within the same layer. Finally, for V dopants at $c = 12\%$ impurity concentration, we find values of $T_c' \approx 28\,\mathrm{K}$ with Eq. (4), which almost exactly reproduces the experimental value of 30 K [42] compared to the overestimation by a factor $T_c/T_c^{\mathrm{exp}} \approx 2$ when using the full summation in Eq. (3). Thus, proper treatment of the magnetic ordering would include all these effects of the impurity distribution, e.g., in form of Monte-Carlo simulations for large supercells that explicitly take into account the percolation threshold of the different impurities at varying concentrations. However, this would go beyond the scope of our present study.

In summary, in our estimation for the magnetic order, we find that co-doping of Cr with Ti, V, Mo, or Nb or doping purely with 4d impurities like Nb and Mo can also lead to stable ferromagnetic ordering as indicated by large values of the mean-field T_c. In contrast, configurations with Mn, Fe, Co, or Ni impurities generally lead to antiferromagnetic order. From the study of dilute magnetic semiconductors [46] it is known that different exchange interactions generally compete in magnetically doped crystals. This was also found in previous studies for V- and Cr-doped TI materials [23]. Our present work shows that impurities in structural proximity dominate the behavior of the T_c, leading us to conclude that the direct overlap of impurity wavefunctions and the virtual hopping of electrons between the impurity atoms via a connecting Te atom in the $\mathrm{Bi_2Te_3}$ matrix plays a pivotal role. This finding, combined with the varying orbital occupation of the d shell of the transition metal impurities evident from the DOS in Figs. 4(a) and 4(b), leads us to conclude that the well-known super- and double-exchange mechanisms [46] are also at play here and are the driving forces behind the magnetic ordering.

E. Transferability to other TI systems

In this subsection, we argue that other TI host systems of the same class of materials, namely $\mathrm{Bi_2Se_3}$ and $\mathrm{Sb_2Te_3}$, show similar trends in the exchange interactions due to magnetic dopants. We infer this from the identical crystal symmetry and the isoelectronic substitution of Bi by Sb or Te by Se compared to the $\mathrm{Bi_2Te_3}$ primarily studied in this paper. We therefore expect a similar Fermi surface of all hosts and a similar chemical bonding of the impurities embedded in all tetradymite TI materials. Probably the biggest difference between these materials is found in the electronic structure of $\mathrm{Bi_2Te_3}$ and $\mathrm{Bi_2Se_3}$ with the dispersion along k_z being less pronounced in the latter. Ultimately, this leads to much weaker hexagonal warping of its topological surface state at surfaces [47]. Despite this difference in the electronic structure of the host, the impurities embedded in $\mathrm{Bi_2Se_3}$ behave very similarly to those embedded in $\mathrm{Bi_2Te_3}$. This can be seen, for instance, in the magnetic moments of the single impurities shown in Fig. A7 of the Supplemental Material [30]. This finding then also transfers to the exchange interaction parameters given in Fig. A8 of the Supplemental Material [30], reported for 3d magnetic impurity dimers embedded into $\mathrm{Bi_2Se_3}$. Consequently, the mean-field T_c for 3d impurities in $\mathrm{Bi_2Se_3}$ shown in the inset of Fig. 8(b) recovers the same chemical trends of preferred magnetic order switching from ferro- to antiferromagnetic coupling with increasing d state filling of the impurities but with values of the T_c that are on average $\sim$200 K/c smaller in Bi_2Se_3 as shown in Fig. A9 of the Supplemental Material [30]. We can therefore conclude that our detailed analysis carried out for Bi_2Te_3 is transferable to other TIs of this material family.

IV. CONCLUSION

In this work, we have presented a computational database of impurity dimers embedded into the topological insulators Bi_2Te_3 and Bi_2Se_3 based on high-throughput density-functional theory calculations. We have analyzed the impurities' DOS and exchange splitting and find a high magnetic polarizability by adjacent magnetic atoms of some transition metal impurities (Rh, Pd), which are nonmagnetic as single defects. Our calculations of the Heisenberg exchange coupling constants reveal the chemical trends with regard to the impurities' d shell filling. We find an overall exponential decay of the J_{ij}'s with distance between the impurities with notable exceptions at special distances where the J_{ij}'s are significantly larger in magnitude. This is traced back to the geometry of the TI's host crystal structure.

From the trends in the long-range magnetic ordering, we conclude that co-doping of Cr with other magnetic impurities like Ti, V, Mo, or Nb is a viable strategy to strengthen ferromagnetic ordering, which might lead to more stable QAH materials. Other impurity configurations with Mn or Fe generally favor antiferromagnetic interactions, which could be useful in the context of axion insulators. In the field of topological quantum computing, a different design strategy in MTIs might also be useful. In contrast to the QAH field where the most stable ferromagnetic ordering is sought after, a smaller exchange splitting or (partial) antiferromagnetic couplings that could effectively weaken the pair-breaking potential for Cooper pairs in the proximity to a superconductor (SC) might be beneficial to optimize the proximity effect in MTI/SC interfaces. While the material trends we find could serve as a guide to future experiments, an experimental realization might be more complex. For instance, co-doping of Cr and V in Sb_2Te_3 can lead to the formation of undesired Cr_2Te_3 instead of the random alloying that we assume here [48]. Therefore, additional studies are necessary in the active field of MTI materials.

The complete dataset for this paper, which includes the full data provenance of all calculations and the scripts used in the data analysis, is made publicly available in the materials cloud repository [49]. The source codes of the `JuKKR` code and the AiiDA-KKR and AiiDA-JuTools plugins are available as open-source repositories from Refs. [21,33,35].

ACKNOWLEDGMENTS

We thank Prof. Phivos Mavropoulos for valuable discussions. We acknowledge the financial support of the Bavarian Ministry of Economic Affairs, Regional Development and Energy within the High-Tech Agenda Project "Bausteine für das Quantencomputing auf Basis topologischer Materialien mit experimentellen und theoretischen Ansätzen." This work was performed as part of the Helmholtz School for Data Science in Life, Earth and Energy (HDS-LEE) and received funding from the Deutsche Forschungsgemeinschaft (DFG, German Research Foundation) under Germany's Excellence Strategy – Cluster of Excellence Matter and Light for Quantum Computing (ML4Q) EXC 2004/1 – 390534769, and from the Helmholtz Association of German Research Centres, and from the European Joint Virtual Lab on Artificial Intelligence, Data Analytics and Scalable Simulation (AIDAS). The authors are, furthermore, grateful for the computing time granted through JARA on the supercomputer JURECA [50] at Forschungszentrum Jülich (project ID "superint") as well as computing time granted by the JARA Vergabegremium and provided on the JARA Partition part of the supercomputer CLAIX at RWTH Aachen University (project ID "jara0191").

R.M., D.A.S., and P.R. developed the `combine_imps_wc` workchain used for the impurity dimer calculations in this work. R.M., J.W., and P.R. analyzed the data. P.R. and S.B. designed the study and P.R. wrote the manuscript with the help of all coauthors.

[1] M. Z. Hasan and C. L. Kane, *Colloquium*: Topological insulators, Rev. Mod. Phys. **82**, 3045 (2010).

[2] Y. Tokura, K. Yasuda, and A. Tsukazaki, Magnetic topological insulators, Nat. Rev. Phys. **1**, 126 (2019).

[3] B. Bernevig, C. Felser, and H. Beidenkopf, Progress and prospects in magnetic topological materials, Nature (London) **603**, 41 (2022).

[4] C. Z. Chang, J. Zhang, X. Feng, J. Shen, Z. Zhang, M. Guo, K. Li, Y. Ou, P. Wei, L. L. Wang, Z. Q. Ji, Y. Feng, S. Ji, X. Chen, J. Jia, X. Dai, Z. Fang, S. C. Zhang, K. He, Y. Wang *et al.*, Experimental observation of the quantum anomalous Hall effect in a magnetic topological Insulator, Science **340**, 167 (2013).

[5] C. Z. Chang, W. Zhao, D. Y. Kim, H. Zhang, B. A. Assaf, D. Heiman, S. C. Zhang, C. Liu, M. H. Chan, and J. S. Moodera, High-precision realization of robust quantum anomalous Hall state in a hard ferromagnetic topological insulator, Nat. Mater. **14**, 473 (2015).

[6] X. Kou, Y. Fan, M. Lang, P. Upadhyaya, and K. L. Wang, Magnetic topological insulators and quantum anomalous Hall effect, Solid State Commun. **215-216**, 34 (2015).

[7] A. J. Bestwick, E. J. Fox, X. Kou, L. Pan, K. L. Wang, and D. Goldhaber-Gordon, Precise quantization of the anomalous Hall effect near zero magnetic field, Phys. Rev. Lett. **114**, 187201 (2015).

[8] S. Grauer, S. Schreyeck, M. Winnerlein, K. Brunner, C. Gould, and L. W. Molenkamp, Coincidence of superparamagnetism and perfect quantization in the quantum anomalous Hall state, Phys. Rev. B **92**, 201304(R) (2015).

[9] C.-Z. Chang, C.-X. Liu, and A. H. MacDonald, *Colloquium*: Quantum anomalous Hall effect, Rev. Mod. Phys. **95**, 011002 (2023).

[10] Y. Deng, Y. Yu, M. Z. Shi, Z. Guo, Z. Xu, J. Wang, X. H. Chen, and Y. Zhang, Quantum anomalous Hall effect in intrinsic magnetic topological insulator $MnBi_2Te_4$, Science **367**, 895 (2020).

[11] T. Li, S. Jiang, B. Shen, Y. Zhang, L. Li, Z. Tao, T. Devakul, K. Watanabe, T. Taniguchi, L. Fu, J. Shan, and K. Mak, Quantum anomalous Hall effect from intertwined moiré bands, Nature (London) **600**, 641 (2021).

[12] M. Mogi, R. Yoshimi, A. Tsukazaki, K. Yasuda, Y. Kozuka, K. S. Takahashi, M. Kawasaki, and Y. Tokura, Magnetic modulation doping in topological insulators toward higher-temperature quantum anomalous Hall effect, Appl. Phys. Lett. **107**, 182401 (2015).

[13] Y. Ou, C. Liu, G. Jiang, Y. Feng, D. Zhao, W. Wu, X. X. Wang, W. Li, C. Song, L. L. Wang, W. Wang, W. Wu, Y. Wang, K. He, X. C. Ma, and Q. K. Xue, Enhancing the quantum anomalous Hall effect by magnetic codoping in a topological insulator, Adv. Mater. **30**, 1703062 (2018).

[14] Y. Fan, P. Upadhyaya, X. Kou, M. Lang, S. Takei, Z. Wang, J. Tang, L. He, L. T. Chang, M. Montazeri, G. Yu, W. Jiang, T. Nie, R. N. Schwartz, Y. Tserkovnyak, and K. L. Wang, Magnetization switching through giant spin–orbit torque in a magnetically doped topological insulator heterostructure, Nat. Mater. **13**, 699 (2014).

[15] J. Wang, B. Lian, X.-L. Qi, and S.-C. Zhang, Quantized topological magnetoelectric effect of the zero-plateau quantum anomalous Hall state, Phys. Rev. B **92**, 081107(R) (2015).

[16] D. Zhuo, Z.-J. Yan, Z.-T. Sun, L.-J. Zhou, Y.-F. Zhao, R. Zhang, R. Mei, H. Yi, K. Wang, M. Chan, C.-X. Liu, K. Law, and C.-Z. Chang, Axion insulator state in hundred-nanometer-thick magnetic topological insulator sandwich heterostructures, Nat. Commun. **14**, 7596 (2023).

[17] P. Rüßmann, F. Bertoldo, and S. Blügel, The AiiDA-KKR plugin and its application to high-throughput impurity embedding into a topological insulator, npj Comput. Mater. **7**, 13 (2021).

[18] https://go.fzj.de/judit

[19] S. H. Vosko, L. Wilk, and M. Nusair, Accurate spin-dependent electron liquid correlation energies for local spin density calculations: a critical analysis, Can. J. Phys. **58**, 1200 (1980).

[20] H. Ebert, D. Ködderitzsch, and J. Minár, Calculating condensed matter properties using the KKR-Green's function method – recent developments and applications, Rep. Prog. Phys. **74**, 096501 (2011).

[21] P. Rüßmann, D. Antognini Silva, D. S. G. Bauer, P. Baumeister, M. Bornemann, J. Bouaziz, S. Brinker, J. Chico, P. H. Dederichs, B. H. Drittler, F. Dos Santos, M. dos Santos Dias, N. Essing, G. Géranton, I. Klepetsanis, A. Kosma, N. H. Long, S. Lounis, P. Mavropoulos, E. Mendive Tapia *et al.*, JuDFTteam/JuKKR: v3.6, Zenodo (2022), doi:10.5281/zenodo.7284738.

[22] P. Sessi, P. Rüßmann, T. Bathon, A. Barla, K. A. Kokh, O. E. Tereshchenko, K. Fauth, S. K. Mahatha, M. A. Valbuena, S. Godey, F. Glott, A. Mugarza, P. Gargiani, M. Valvidares, N. H. Long, C. Carbone, P. Mavropoulos, S. Blügel, and M. Bode, Superparamagnetism-induced mesoscopic electron focusing in topological insulators, Phys. Rev. B **94**, 075137 (2016).

[23] T. R. Peixoto, H. Bentmann, P. Rüßmann, A. V. Tcakaev, M. Winnerlein, S. Schreyeck, S. Schatz, R. C. Vidal, F. Stier, V. Zabolotnyy, R. J. Green, C. H. Min, C. I. Fornari, H. Maaß, H. B. Vasili, P. Gargiani, M. Valvidares, A. Barla, J. Buck, M. Hoesch *et al.*, Non-local effect of impurity states on the exchange coupling mechanism in magnetic topological insulators, npj Quantum Mater. **5**, 87 (2020).

[24] A. Tcakaev, V. B. Zabolotnyy, C. I. Fornari, P. Rüßmann, T. R. F. Peixoto, F. Stier, M. Dettbarn, P. Kagerer, E. Weschke, E. Schierle, P. Bencok, P. H. O. Rappl, E. Abramof, H. Bentmann, E. Goering, F. Reinert, and V. Hinkov, Incipient antiferromagnetism in the Eu-doped topological insulator Bi_2Te_3, Phys. Rev. B **102**, 184401 (2020).

[25] S. Nakajima, The crystal structure of $Bi_2Te_{3-x}Se_x$, J. Phys. Chem. Solids, **24** 479 (1963).

[26] R. W. G. Wyckoff, *Crystal Structures*, 2 ed. (John Wiley and Sons, New York, USA, 1964).

[27] N. Stefanou, H. Akai, and R. Zeller, An efficient numerical method to calculate shape truncation functions for Wigner-Seitz atomic polyhedra, Comput. Phys. Commun. **60**, 231 (1990).

[28] N. Stefanou and R. Zeller, Calculation of shape-truncation functions for Voronoi polyhedra, J. Phys.: Condens. Matter **3**, 7599 (1991).

[29] R. Zeller, An elementary derivation of Lloyd's formula valid for full-potential multiple-scattering theory, J. Phys.: Condens. Matter **16**, 6453 (2004).

[30] See Supplemental Material at http://link.aps.org/supplemental/10.1103/PhysRevMaterials.8.104201 for an illustration of the geometries and J_{ij} maps of the impurity dimers at larger distances, distance-dependent inter-QL vs intra-QL contributions to the J_{ij}'s, the resulting mean-field T_c from inter-QL and intra-QL contributions, convergence plots of the J_{ij} calculations, and the corresponding results for Bi_2Se_3.

[31] D. S. G. Bauer, Development of a relativistic full-potential first-principles multiple scattering Green function method applied to complex magnetic textures of nano structures at surfaces, Ph.D. thesis, RWTH Aachen University, 2013.

[32] A. Liechtenstein, M. Katsnelson, V. Antropov, and V. Gubanov, Local spin density functional approach to the theory of exchange interactions in ferromagnetic metals and alloys, J. Magn. Magn. Mater. **67**, 65 (1987).

[33] P. Rüßmann, D. Antognini Silva, R. Aliberti, J. Bröder, H. Janssen, R. Mozumder, M. Struckmann, J. Wasmer, and S. Blügel, JuDFTteam/aiida-kkr: v2.1.0. Zenodo (2023), doi:10.5281/zenodo.3628250.

[34] S. P. Huber, S. Zoupanos, M. Uhrin, L. Talirz, L. Kahle, R. Häuselmann, D. Gresch, T. Müller, A. V. Yakutovich, C. W. Andersen, F. F. Ramirez, C. S. Adorf, F. Gargiulo, S. Kumbhar, E. Passaro, C. Johnston, A. Merkys, A. Cepellotti, N. Mounet, N. Marzari *et al.*, AiiDA 1.0, a scalable computational infrastructure for automated reproducible workflows and data provenance, Sci. Data **7**, 300 (2020).

[35] J. Wasmer, R. Kovacic, and P. Rüßmann, JuDFTteam/aiida-jutools: v0.1.2, Zenodo (2023), doi:10.5281/zenodo.10429636.

[36] D. Di Miceli, E. Zsurka, J. Legendre, K. Moors, T. L. Schmidt, and L. Serra, Conductance asymmetry in proximitized magnetic topological insulator junctions with majorana modes, Phys. Rev. B **108**, 035424 (2023).

[37] J. Legendre, E. Zsurka, D. Di Miceli, L. Serra, K. Moors, and T. L. Schmidt, Topological properties of finite-size

heterostructures of magnetic topological insulators and superconductors, arXiv:2404.16520.

[38] Note that for Ru max $|\Delta m_1| > m$ because for Ru–Nb the Ru moment increases in magnitude but also flips the sign to an antiparallel alignment with respect to the Nb moment.

[39] E. Koch, *Correlated Electrons: From Models to Materials Modeling and Simulation* (Forschungszentrum Jülich GmbH Zenralbibliothek, Verlag, Jülich, 2012), Chap. Exchange Mechanisms.

[40] M. Pajda, J. Kudrnovský, I. Turek, V. Drchal, and P. Bruno, *Ab initio* calculations of exchange interactions, spin-wave stiffness constants, and curie temperatures of Fe, Co, and Ni, Phys. Rev. B **64**, 174402 (2001).

[41] Note that the prefactor here is $1/3$ instead of $2/3$ due to the different definition of the Heisenberg Hamiltonian Eq. (2) that contains a factor $1/2$ in our work.

[42] X. Kou, S.-T. Guo, Y. Fan, L. Pan, M. Lang, Y. Jiang, Q. Shao, T. Nie, K. Murata, J. Tang, Y. Wang, L. He, T.-K. Lee, W.-L. Lee, and K. L. Wang, Scale-invariant quantum anomalous Hall effect in magnetic topological insulators beyond the two-dimensional limit, Phys. Rev. Lett. **113**, 137201 (2014).

[43] J. Checkelsky, R. Yoshimi, A. Tsukazaki, K. Takahashi, Y. Kozuka, J. Falson, M. Kawasaki, and Y. Tokura, Trajectory of the anomalous Hall effect towards the quantized state in a ferromagnetic topological insulator, Nat. Phys. **10**, 731 (2014).

[44] In contrast to Eq. (3), the summation starts at $j = 2$ instead of $j = 1$.

[45] Y. S. Hor, P. Roushan, H. Beidenkopf, J. Seo, D. Qu, J. G. Checkelsky, L. A. Wray, D. Hsieh, Y. Xia, S.-Y. Xu, D. Qian, M. Z. Hasan, N. P. Ong, A. Yazdani, and R. J. Cava, Development of ferromagnetism in the doped topological insulator $Bi_{2-x}Mn_xTe_3$, Phys. Rev. B **81**, 195203 (2010).

[46] K. Sato, P. H. Dederichs, H. Katayama-Yoshida, and J. Kudrnovský, Exchange interactions in diluted magnetic semiconductors, J. Phys.: Condens. Matter **16**, S5491 (2004).

[47] E. Zsurka, C. Wang, J. Legendre, D. Di Miceli, L. Serra, D. Grützmacher, T. L. Schmidt, P. Rüßmann, and K. Moors, Low-energy modeling of three-dimensional topological insulator nanostructures, Phys. Rev. Mater. **8**, 084204 (2024).

[48] L. B. Duffy, A. I. Figueroa, G. van der Laan, and T. Hesjedal, Codoping of Sb_2Te_3 thin films with V and Cr, Phys. Rev. Mater. **1**, 064409 (2017).

[49] R. Mozumder, J. Wasmer, D. Antognini Silva, S. Blügel, and P. Rüßmann, Dataset to "High-throughput magnetic co-doping and design of exchange interactions in topological insulators", Mater. Cloud Archive 2024, 141 (2024).

[50] P. Thörnig, JURECA: Data Centric and Booster Modules implementing the Modular Supercomputing Architecture at Jülich Supercomputing Centre, J. Large-Scale Res. Facilities **7**, A182 (2021).